BULLETIN OF THE POLISH ACADEMY OF SCIENCES
TECHNICAL SCIENCES, Vol. 68, No. 1, 2020
DOI: 10.24425/bpasts.2020.131834



# ITO layer as an optical confinement for nitride edge-emitting lasers

M. KUC, A.K. SOKÓŁ*, Ł. PISKORSKI, M. DEMS, M. WASIAK, R.P. SARZAŁA, and T. CZYSZANOWSKI

Institute of Physics, Lodz University of Technology, 219 Wólczańska St., 90-924 Łódź, Poland

**Abstract.** This paper presents the results of a numerical analysis of nitride-based edge-emitting lasers with an InGaN/GaN active region designed for continuous wave room temperature emission of green and blue light. The main goal was to investigate whether the indium thin oxide (ITO) layer can serve as an effective optical confinement improving operation of these devices. Simulations were performed with the aid of a self-consistent thermal-electrical-optical model. Results obtained for green- and blue-emitting lasers were compared. The ITO layer in the p-type cladding was found to effectively help confine the laser mode in the active regions of the devices and to decrease the threshold current density.

**Key words:** edge-emitting lasers, InGaN/GaN, computer simulation, ITO, optical confinement.

## 1. Introduction

Currently, in order to achieve lasing threshold III-N-based continuous wave (CW), edge-emitting lasers (EELs) operating at room temperature (RT) in the green spectral range require significantly higher current densities than analogous devices generating blue light [1, 2]. The primary reason for this is the rather low differential gain caused by spectral broadening and the low transition matrix element. Another problem is the presence of AlGaN layers in the laser active region. Aluminum is highly susceptible to oxidation, which causes degradation of the device. Moreover, AlGaN layers (p-AlGaN in particular) must be grown at a higher temperature, which exposes the quantum wells to additional thermal stress and may impair their properties. Finally, high-resistance p-AlGaN layers increase the overall electrical resistance of the device, so a higher supply voltage is required. This causes more intense heating of the device, which in turn decreases its performance. Therefore, the removal of aluminum from the laser structure may have advantages. On the other hand, removing AlGaN cladding layers weakens optical mode confinement in the active region of the laser and increases the threshold current density. Using InGaN layers to form the waveguide could solve this problem. However, increasing the indium content or the thickness of the InGaN layers generates additional strain within the semiconductor structure, especially when it is grown on semipolar GaN substrates [3, 4]. New design solutions are therefore sought that would allow to effectively confine the laser mode in the active region and thereby improve the performance of edge-emitting lasers generating green light. One of the most interesting approaches consists of the partial replacement of p-type gallium nitride (p-GaN) in the waveguide layers with indium tin oxide (ITO) [5]. The low refractive index of ITO prevents the optical field from penetrating p-type magnesium-doped layers with a high absorption coefficient and thus enables the current density required to obtain laser action to be decreased.

This paper presents the results of a numerical analysis showing the impact of the ITO layer on the lasing threshold of a semipolar nitride CW edge-emitting laser designed to generate green light ($\lambda = 540$ nm) at RT. For comparison, the results for an analogous device emitting blue light ($\lambda = 480$ nm) are also discussed.

## 2. Material parameters

Simulations of nitride-based green- and blue-emitting lasers were performed with the aid of the self-consistent thermal-electrical-optical-gain model, descriptions of which can be found in [6–9]. The following subsections detail the material parameters used in the calculations.

**2.1. Thermal and electrical conductivities.** Table 1 presents the thermal and electrical conductivities of the (Al,In)GaN materials [6] and metals [7]. The impact of size-effects and impurities on the thermal conductivity of GaN, as reported recently in [10] and discussed in [6], was also taken into account in the simulations. Thermal and electrical conductivities of ITO were assumed based on data from [11].

**2.2. Refractive index and absorption coefficient.** Table 2 displays the material parameters used in the optical calculations. The refractive index of $Al_{0.2}Ga_{0.8}N$ was taken from [12, 13]. The refractive index and absorption coefficient of $Al_{0.83}In_{0.17}N$ (lattice-matched to GaN) is from [14]. The absorption coefficient for the n-type (In)GaN materials was estimated based on [15, 16] and the Drude model [17] to be 10 $cm^{-1}$. The absorption coefficient for all p-type (Al,In)GaN layers was assumed based on [8, 15, 17] to be 100 $cm^{-1}$.

*e-mail: adam.sokol@p.lodz.pl

Manuscript submitted 2019-08-25, revised 2019-11-08, initially accepted for publication 2019-11-22, published in February 2020

Table 1
Thermal and electrical parameters of materials used in simulations. $\kappa_{300K}$ and $\kappa_{400K}$ – thermal conductivity at 300 K and 400 K, $\sigma_{300K}$ and $\sigma_{400K}$ – electrical conductivity at 300 K and 400 K, QW – quantum well

| Material | Doping [cm$^{-3}$] | Thickness [μm] | $\kappa_{300K}$ [W/(m·K)] | $\kappa_{400K}$ [W/(m·K)] | $\sigma_{300K}$ [S/m] | $\sigma_{400K}$ [S/m] |
|---|---|---|---|---|---|---|
| p-GaN | Mg: $2\cdot10^{19}$ | 0.30 | 92 | 61 | 95 | 309 |
| p-$In_{0.06}Ga_{0.94}N$ | Mg: $1\cdot10^{19}$ | 0.07 | 31 | 26 | 362 | 353 |
| p-$In_{0.08}Ga_{0.92}N$ | Mg: $1\cdot10^{19}$ | 0.045 | 23 | 20 | 284 | 280 |
| p-$Al_{0.2}Ga_{0.8}N$ | Mg: $5\cdot10^{19}$ | 0.010 | 13 | 12 | 22 | 70 |
| n-GaN (substrate) | Si: $2\cdot10^{18}$ | 50 | 166 | 110 | $7.9\cdot10^{3}$ | $7.4\cdot10^{3}$ |
| n-$In_{0.06}Ga_{0.94}N$ | Si: $5\cdot10^{18}$ | 0.03 | 30 | 25 | 807 | 889 |
| n-$In_{0.08}Ga_{0.92}N$ | Si: $5\cdot10^{18}$ | 0.01 | 28 | 26 | 636 | 703 |
| GaN (barrier) | undoped | 0.010 | 61 | 41 | 255 | 242 |
| n-$In_{0.18}Ga_{0.82}N$ (QW) | Si-doped | 0.0045 | 7 | 6 | 337 | 375 |
| n-$In_{0.29}Ga_{0.71}N$ (QW) | Si-doped | 0.0027 | 2 | 2 | 250 | 278 |
| $SiO_2$ | n/a | 0.25 | 1 | 1 | $1\cdot10^{-13}$ | $1\cdot10^{-13}$ |
| ITO | n/a | 0.25 | 3 | 3 | $1\cdot10^{6}$ | $1\cdot10^{6}$ |
| Au | n/a | 1 | 316 | 311 | $4.4\cdot10^{7}$ | $3.2\cdot10^{7}$ |
| Al | n/a | 0.03 | 180 | 180 | $3.8\cdot10^{7}$ | $3.8\cdot10^{7}$ |
| Ti | n/a | 0.03 | 22 | 20 | $2.2\cdot10^{6}$ | $1.6\cdot10^{6}$ |
| PbSn | n/a | 1 | 50 | 50 | $6\cdot10^{6}$ | $6\cdot10^{6}$ |
| Cu | n/a | 5000 | 403 | 393 | $5.8\cdot10^{7}$ | $4.2\cdot10^{7}$ |

Table 2
Optical parameters of materials used in simulations. $n_{r,300K}$ and $n_{r,400K}$ – refractive index at 300 K and 400 K, $\alpha_{300K}$ and $\alpha_{400K}$ – absorption coefficient at 300 K and 400 K, QW – quantum well. For green laser: $x = 0.08$, $y = 0.29$. For blue laser: $x = 0.06$, $y = 0.18$

| Material | Green laser (540 nm) | | | | Blue laser (480 nm) | | | |
|---|---|---|---|---|---|---|---|---|
| | $n_{r,300K}$ | $n_{r,400K}$ | $\alpha_{300K}$ [1/cm] | $\alpha_{400K}$ [1/cm] | $n_{r,300K}$ | $n_{r,400K}$ | $\alpha_{300K}$ [1/cm] | $\alpha_{400K}$ [1/cm] |
| p-GaN | 2.3787 | 2.3881 | 100 | 100 | 2.4175 | 2.4289 | 100 | 100 |
| p-$In_xGa_{1-x}N$ | 2.4429 | 2.4530 | 100 | 100 | 2.4843 | 2.4966 | 100 | 100 |
| p-$Al_{0.2}Ga_{0.8}N$ | 2.3099 | 2.3181 | 100 | 100 | 2.3410 | 2.3507 | 100 | 100 |
| n-GaN | 2.3787 | 2.3881 | 10 | 10 | 2.4175 | 2.4289 | 10 | 10 |
| n-$In_xGa_{1-x}N$ | 2.4429 | 2.4530 | 10 | 10 | 2.4843 | 2.4966 | 10 | 10 |
| n-$In_yGa_{1-y}N$ (QW) | 2.7310 | 2.7431 | gain | gain | 2.7588 | 2.7728 | gain | gain |
| $SiO_2$ | 1.4795 | 1.4795 | 0 | 0 | 1.4828 | 1.4828 | 0 | 0 |
| ITO | 1.9357 | 1.9357 | 1920 | 1920 | 1.9786 | 1.9786 | 2180 | 2180 |
| Au | 0.3710 | 0.3710 | $4.9\cdot10^{5}$ | $4.9\cdot10^{5}$ | 1.1890 | 1.1890 | $4.7\cdot10^{5}$ | $4.7\cdot10^{5}$ |
| Ti | 2.5081 | 2.5081 | $8.0\cdot10^{5}$ | $8.0\cdot10^{5}$ | 2.3346 | 2.3346 | $8.3\cdot10^{5}$ | $8.3\cdot10^{5}$ |

The impact of temperature on absorption was not taken into consideration in the simulations.

Based on the refractive index of GaN reported in [18], the refractive indices of InGaN (In: 0.105, 0.115, 0.12, 0.15, 0.24, 0.25) measured at a wavelength of 600 nm [19] and formula (1) presented in [20] for the refractive index of InGaN as a function of photon energy $E$:

$$n_{r,\mathrm{InGaN}}(E) = n_{r,\mathrm{GaN}}(E - \Delta E), \tag{1}$$

the energy shift $\Delta E$ was calculated as a function of the indium molar fraction $x$ in $In_xGa_{1-x}N$ (Fig. 1a, dashed line):

$$\Delta E = 6.2 \cdot x^2 - 5.9 \cdot x. \tag{2}$$

In Fig. 1b, the dotted line illustrates the refractive index of $In_{0.15}Ga_{0.85}N$, taking into account the energy shift between the GaN and $In_{0.15}Ga_{0.85}N$ band gaps, as originally proposed in [20]. The dashed line shows the refractive index dependence

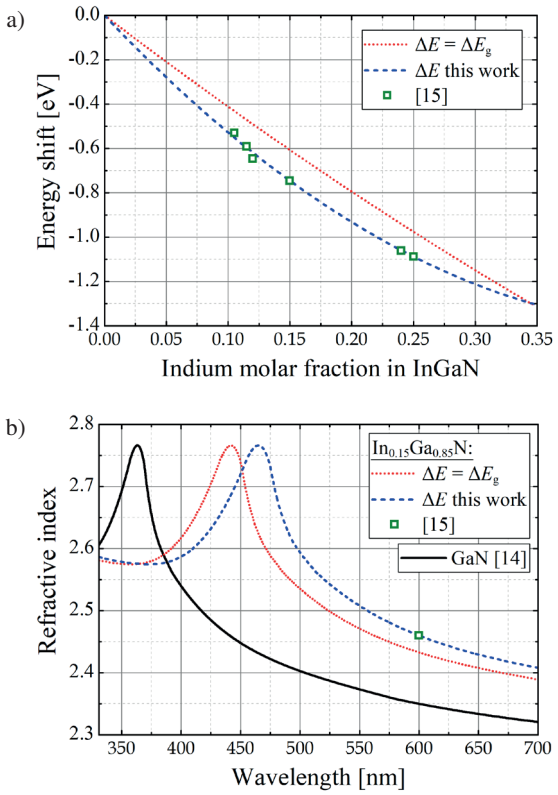


Fig. 1. Calculated energy shift $\Delta E$ (a) and refractive index spectra (b) for GaN and InGaN. $\Delta E_g$ – band gap shift

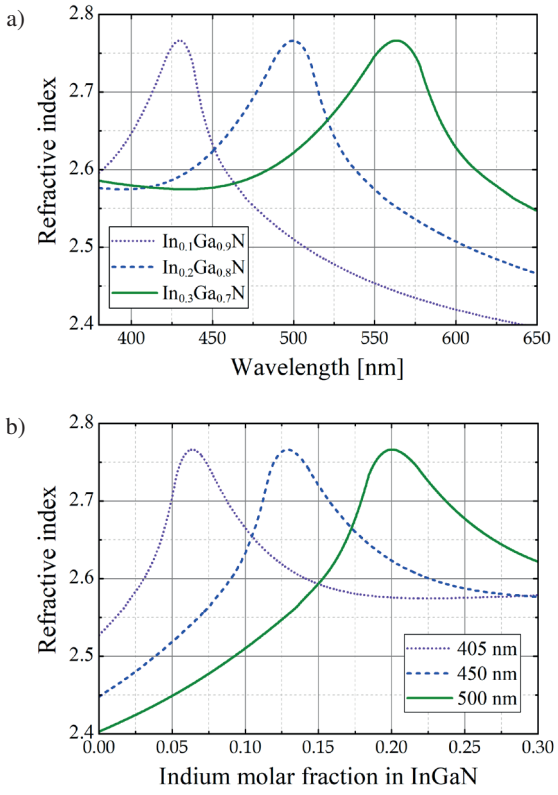


Fig. 2. InGaN refractive index calculated as a function of wavelength (a) and indium molar fraction (b)

used in the calculations, which reflects the refractive index spectral dependence proposed in [20] and crosses the value of the $In_{0.15}Ga_{0.85}N$ refractive index found experimentally in [19].

Given the refractive index spectra for GaN [18], the refractive indices of InGaN at a wavelength of 600 nm [19] and the formula for energy shift (2), the refractive index of InGaN can be calculated for a wide range of wavelengths and indium molar fractions (Fig. 2). The respective temperature dependencies of the refractive indices of GaN and InN are given in [10] and [21]. To obtain the temperature coefficient of InGaN, linear approximation between the temperature coefficients of GaN and InN was used.

**2.3. Diffusion and recombination coefficients.** The carrier density profile within the active region was determined using a diffusion equation at lasing threshold [22]. The RT ambipolar diffusion coefficient $D$ was assumed to be 2 $cm^2s^{-1}$ [23–26]. Based on experimental data presented in [26], the ambipolar diffusion coefficient as a function of temperature can be found using the following approximation formula:

$$D(T) = 2 \cdot (300\ \mathrm{K}/T)\,\mathrm{cm^2 s^{-1}}. \tag{3}$$

The RT value for the monomolecular recombination coefficient $A$ was assumed to be $4{\cdot}10^7$ $s^{-1}$. This is about three times higher than the average value for polar devices [27–31], and is in line with data presented in [32]. Taking into account the experimentally determined temperature dependence of the monomolecular recombination coefficient presented in [33], the following formula, which may be used to calculate $A$ for a given temperature, was derived:

$$A(T) = 4 \cdot 10^7 \cdot (T/300\ \mathrm{K})^{3.8}\,\mathrm{s^{-1}}. \tag{4}$$

The RT value for the bimolecular recombination coefficient $B$ was assumed to be $2{\cdot}10^{-11}$ $cm^3s^{-1}$. This is about two times higher than the average value for polar devices [29, 34], which is consistent with [32]. To take the temperature dependence of this parameter into account, the same relation as given in [35], i.e. $B \propto T^{-1.5}$, was used. Hence the formula for $B$ is:

$$B(T) = 2 \cdot 10^{-11} \cdot (300\ \mathrm{K}/T)^{1.5}\,\mathrm{cm^3 s^{-1}}. \tag{5}$$

Based on experimental measurements, the Auger recombination coefficient $C$ [36] has insignificant dependence on temperature in the 200–450 K range. However, it should be remembered that reducing the energy gap $E_g$ of the material increases the Auger coefficient. This trend also applies to other semiconductor material systems [37]. Instead of considering $C(E_g)$ dependence, a simple formula (6) is proposed based on experimental data reported in [38, 39]. It can be used to determine the value of the Auger recombination coefficient for photon energy $E$ corresponding to the emitted wavelength:

$$C(T) = 1.1 \cdot 10^{-28} \cdot (E/1\ \mathrm{eV})^{-4}\,\mathrm{cm^6 s^{-1}}. \tag{6}$$

The assumed value is lower than the values for semipolar devices reported in [32, 40]. However, for the modeled structures,

Auger recombination has the least influence on laser performance of all recombination processes [41]. For quantum wells with a wide bandgap this process may even be neglected entirely.

## 3. Results

Simulations were carried out for semipolar ridge waveguide lasers designed for emission of green ($\lambda = 540$ nm) and blue ($\lambda = 480$ nm) light, based on the devices described in [5]. The geometrical parameters of the two modeled structures are shown in Table 3 and Fig. 1a, 3a. Henceforth, they are simply referred to as the "green laser" and "blue laser", respectively.

In contrast to paper [5], in which the authors limited their numerical considerations to only optical phenomena, the present paper shows the results of a full self-consistent thermal-electrical-optical-gain analysis. The designs of both lasers were optimized to provide the lowest threshold current density for CW operation at RT.

According to [5], the width of the green laser ridge was assumed to be 2 μm, and that of the blue 7.5 μm. In both cases, the resonator length was equal to 500 μm [42]. The thickness of the GaN substrate was set to 50 μm based on [42]. The lasers were assumed to be mounted pup on copper heat sinks using 1-μm thick PbSn solder. The surface electrical resistances of the p-type (Ti/Au) and n-type (Al/Au) contacts were set to $5{\cdot}10^{-4}$ Ω·cm$^2$ and $5{\cdot}10^{-5}$ Ω·cm$^2$, respectively. Based on [43], it was assumed that these quantities did not depend on the current density.

**3.1. Green laser.** A typical drawback of edge-emission lasers made of III-N materials is related to the high resistance of the p-contact [43]. This causes a significant voltage drop (Fig. 3a) and also contributes to the generation of a large amount of heat over the active area (Fig. 3b), which must be removed from the structure if the device is to work efficiently. Fig. 3a shows that almost three times more voltage was deposited on the p-contact layer than in the active area of the laser: 6.4 V compared to 2.3 V. The maximum temperature within the active area reached 327.7 K and was 9.5 K lower than the temperature of the p-contact (337.2 K). The temperature increase was thus 27.7 K, which at an input power of 3.2 W gives thermal resistance of about 8.7 K/W. The maximum gain in the active area at the lasing threshold was 2181 cm$^{-1}$ for a wavelength of 538.3 nm (Fig. 4a).

Table 3
Modeled structures. EBL stands for electron blocking layer, MQW stands for multi-quantum well

| Layer | Green laser (540 nm) | | Blue laser (480 nm) | |
|---|---|---|---|---|
| | Material | Thickness [μm] | Material | Thickness [μm] |
| p-contact | Ti/Au | 0.03/1 | Ti/Au | 0.03/1 |
| Insulator | $SiO_2$ | 0.25 | $SiO_2$ | 0.25 |
| p-cladding | ITO/p-GaN | 0.28/0.27 | ITO/p-GaN | 0.45/0.10 |
| p-waveguide | p-$In_{0.08}Ga_{0.92}N$ | 0.045 | p-$In_{0.06}Ga_{0.94}N$ | 0.07 |
| EBL | p-$Al_{0.2}Ga_{0.8}N$ | 0.01 | p-$Al_{0.2}Ga_{0.8}N$ | 0.01 |
| Active region | $In_{0.29}Ga_{0.71}N$/GaN MQW | 0.0027/0.01 | $In_{0.18}Ga_{0.82}N$/GaN MQW | 0.0045/0.010 |
| n-waveguide | n-$In_{0.08}Ga_{0.92}N$ | 0.01 | n-$In_{0.06}Ga_{0.94}N$ | 0.03 |
| Substrate | n-GaN | 50 | n-GaN | 50 |
| n-contact | Al/Au | 0.03/0.3 | Al/Au | 0.03/0.3 |

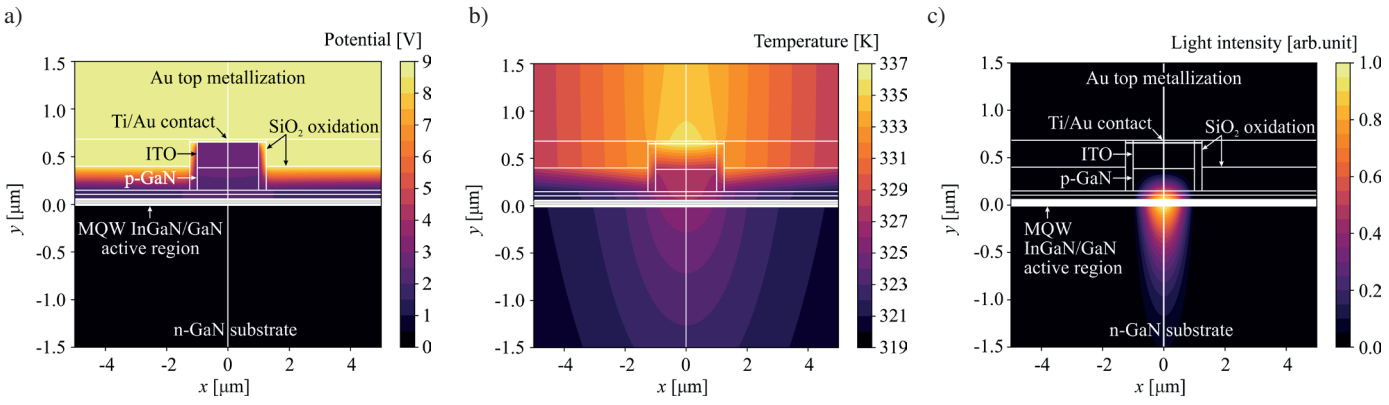


Fig. 3. Distributions of potential (a), temperature (b) and light intensity (c) in the *xy* plane for the green laser at the lasing threshold

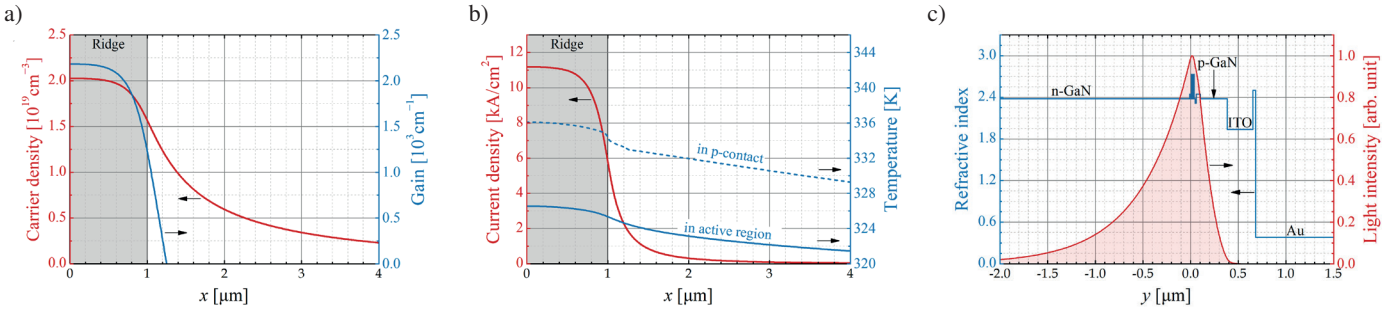


Fig. 4. Lateral distributions of a) carrier density and material gain, b) current density and temperature within the active region and p-contact of the green laser, c) cistribution of refractive index and light intensity along the vertical axis ($x = 0$)

The gain distribution was determined taking into account the influence of temperature and carrier density. The calculated distribution of the threshold current density (Fig. 4b) with a maximum value of 11.31 kA/cm$^2$ is in agreement with the data from [2].

The optical fill factor, defined as the ratio of the integral from the distribution of light intensity in the active region to the integral of the distribution of light intensity in the whole structure along the $y$ axis for $x = 0$, was equal to 7%. Figures 3c and 4c present the distribution of light intensity determined inside the structure. Due to the poor optical confinement on the n side of the structure, the optical mode strongly penetrated into the substrate. The filling factors for p-type and n-type layers were 20% and 73%, respectively.

**3.2. Blue laser.** As with the green laser, the largest increase in temperature in the blue laser took place in the pcontact (Fig. 5b). The temperature of this layer reached 317.3 K (Fig. 6b). The maximum temperature increase within the active area did not exceed 15.2 K with an input power of 2.3 W, which means that the thermal resistance of the structure was equal to 6.6 K/W. The voltage drop across the p-contact was 1.88 V and in the active area 2.55 V (Fig. 5a). The carrier density and material gain at the laser action threshold were equal to $1.2{\cdot}10^{19}$ cm$^{-3}$ and 783 cm$^{-1}$, respectively (Fig. 6a). These values are much smaller than those for the green laser ($2.0{\cdot}10^{19}$ cm$^{-3}$ and 2181 cm$^{-1}$). Figs 5c and 6c present the distributions of light intensity determined inside the structure. A comparison of Fig. 4c and Fig. 6c reveals that the thicker

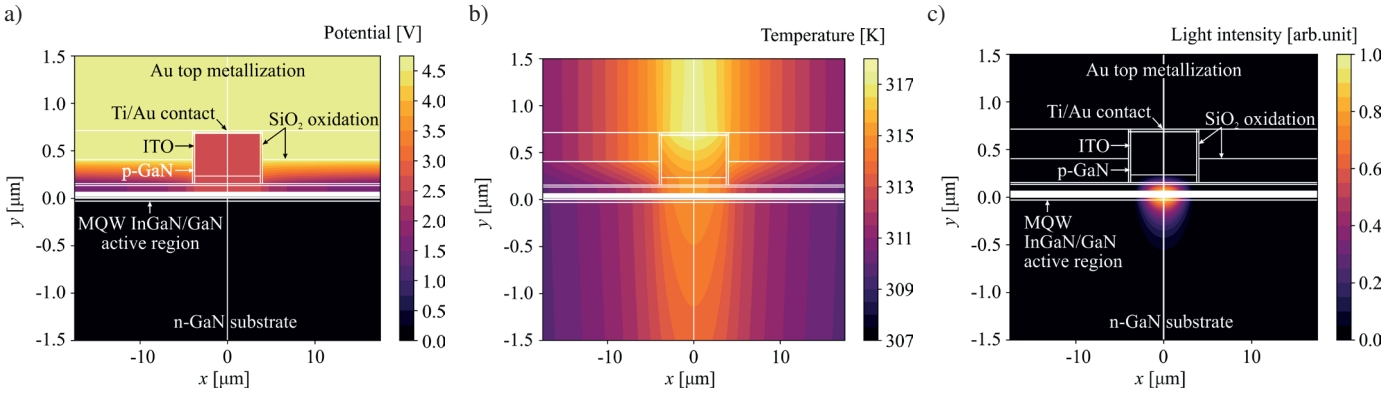


Fig. 5. Distributions of potential (a), temperature (b) and light intensity (c) in the $xy$ plane for the blue laser at the lasing threshold

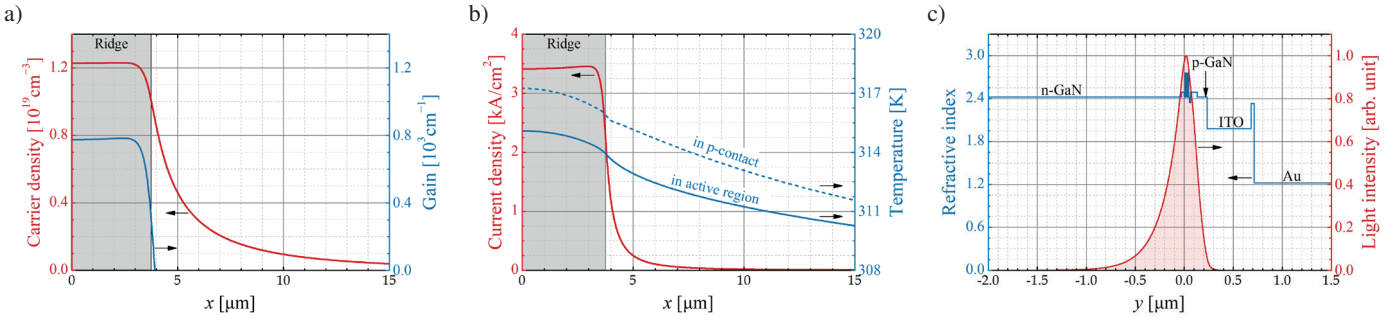


Fig. 6. Lateral distributions of a) carrier density and material gain, b) current density and temperature within the active region and p-contact of the blue laser, c) distribution of refractive index and light intensity along the vertical axis ($x = 0$)

waveguide layers enabled stronger confinement of the lasing mode in the active area on the p side. The fill factor in the active area was 16.2%, more than twice as much as for the green laser. The filling factors for the ptype and ntype layers were equal to 25.3% and 58.5%, respectively.

**3.3. Thickness of the ITO layer.** The green laser described in [5] contains a p-cladding layer with a thickness of 0.55 μm. It consists of a p-GaN layer with a thickness of 0.3 μm and an ITO layer with a thickness of 0.25 μm. As part of the current work, we examined the influence of ITO layer thickness on the threshold current density of this device. The calculations assume that the total thickness of the pcladding was constant and equal to 0.55 μm, so any change in ITO thickness was followed by an appropriate variation in p-GaN thickness. The simulation results for the green laser were shown in Fig. 7a. It can be seen that the smallest current threshold density (11.31 kA/cm$^2$) was obtained for the ITO layer with a thickness of approximately 0.28 μm. Increasing the thickness of the ITO caused the mode to gradually push out of the active area towards the n-type layers, which entailed an increase in the absorption of the emitted radiation and thus an increase in the threshold current density. The reduction in ITO thickness in turn weakened the mode confinement on the p side, which caused the radiation to penetrate more and more into the p-type layers. The absorption coefficient of these layers was ten times greater than that of the n-type layers. This of course resulted in an increase in the threshold current density. The simulations show that without the ITO layer the modeled structure would not reach the lasing threshold.

Analogous calculations were carried out for the blue laser. The results are presented in Fig. 7b. In this case, the optimal ITO thickness was about 0.45 μm. For this thickness, the laser threshold current density was approximately 3.46 kA/cm$^2$. However, one can see that – in contrast to the green laser – modification of the ITO thickness in even a fairly wide range of values had a limited effect on the threshold current density. In the 0.39 to 0.49 μm thickness range, the current density change did not exceed 1.5%. As in the case of the green laser, it was impossible to achieve lasing threshold without the ITO layer.

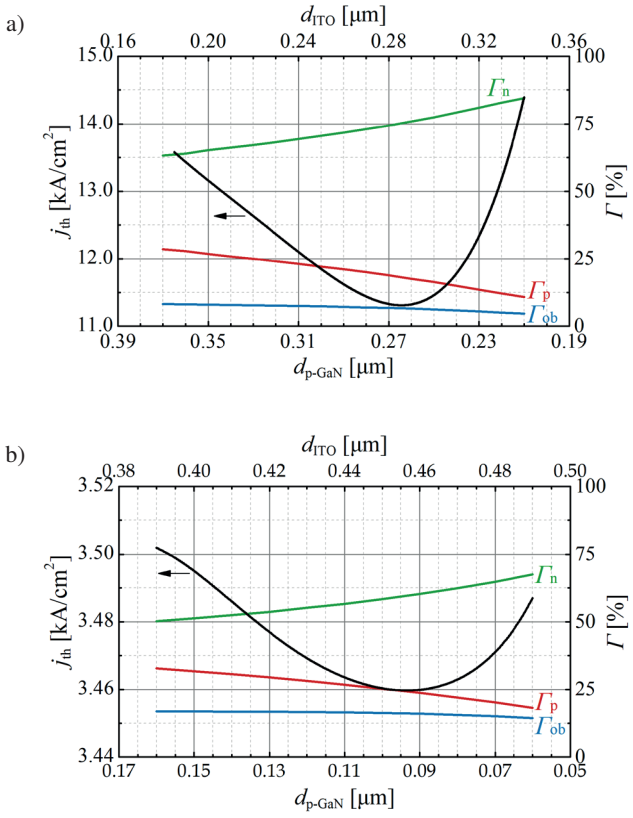


Fig. 7. Threshold current density ($j_{th}$) and confinement factor for the active region ($\Gamma_{ob}$), n-type layers ($\Gamma_n$) and p-type layers ($\Gamma_p$) versus thickness of the ITO ($d_{ITO}$) and p-GaN ($d_{p-GaN}$) layers for the green (a) and blue (b) laser

## 4. Conclusions

This paper has presented simulation results for nitride edge-emitting lasers designed for operation at RT and continuous emission of green (540 nm) or blue (450 nm) light. The weak mode confinement on the n side of the structure and the high absorption of radiation in the ptype layers meant that the green laser required a very high current density to achieve laser action. The use of an ITO layer reduced the penetration of the optical field into the p-GaN layer. Optimal thicknesses for the ITO layers (0.28 μm for the green laser and 0.45 μm for the blue laser), which allowed the lowest possible threshold current densities for the analyzed structures, were determined. These thicknesses were selected in such a way as to prevent the optical field from penetrating into the p-type layers, keeping the largest possible confinement factor within the active area. Nevertheless, the threshold current density for the green laser (11.31 kA/cm$^2$) was more than three times greater than that of the blue laser (3.46 kA/cm$^2$). Further research is required to develop design solutions that could improve the performance of lasers operating in the green spectral range, in particular those that would increase mode confinement on the n side of the structure and prevent the optical field from penetrating into the n-GaN substrate.

**Acknowledgements.** This work was partially supported by the National Science Centre, Poland, under project no. 2015/19/D/ST7/01609. This work is connected to the POIG.01.03.01-00-159 project InTechFun, supported by the European Union under the European Regional Development Fund, through Grant Innovate Economy, and was realized during its development.

## References

[1] Z.C. Feng, *Handbook of Solid-State Lighting and LEDs*, 1st ed., CRC Press, Boca Raton, 2017.

[2] D. Sizov et al., "Development of semipolar laser diode", *Phys. Status Solidi A* 210 (3), 459–465 (2013).

[3] M.T. Hardy et al., "True green semipolar InGaN-based laser diodes beyond critical thickness limits using limited area epitaxy", *J. Appl. Phys.* 114 (18), 183101 (2013).

[4] M. Murayama et al., "Watt-class green (530?nm) and blue (465?nm) laser diodes", *Phys. Status Solidi A* 215 (10), 1700513 (2018).

[5] M.T. Hardy et al., "Indium-tin-oxide clad blue and true green semipolar InGaN/GaN laser diodes", *Appl. Phys. Lett.*, 103 (8), 081103 (2013).

[6] M. Kuc, R.P. Sarzała, and W. Nakwaski, "Thermal crosstalk in arrays of III-N-based Lasers", *Mater. Sci Eng. B* 178 (20), 1395–1402 (2013).

[7] M. Kuc, R.P. Sarzała, S. Stańczyk, and P. Perlin, "Numerical investigation of an impact of a top gold metallization on output power of a p-up III-N-based blue-violet edge-emitting laser diode", *Opto-Electron. Rev.* 23 (2), 131–136 (2015).

[8] M. Kuc et al., "Optical simulations of blue and green semipolar InGaN/GaN lasers", *Proc. SPIE* 10532, 1053228 (2018).

[9] A.K. Sokół, Ł. Piskorski, M. Kuc, M. Wasiak, and R.P. Sarzała, "Concept of the CW GaN-based VECSEL", *Proc. SPIE* 10515, 105150X (2018).

[10] T.E. Beechem et al., "Size dictated thermal conductivity of GaN", *J. Appl. Phys.* 120 (9), 095104 (2016).

[11] L. Wang, J. Wen, C. Yang, and B. Xiong, "Potential of ITO thin film for electrical probe memory applications", *Sci. Technol. Adv. Mater.* 19 (1), 791–801 (2018).

[12] M. Soltani, R. Soref, T. Palacios, and D. Englund, "AlGaN/AlN integrated photonics platform for the ultraviolet and visible spectral range", *Opt. Express* 24 (22), 25415–25423 (2016).

[13] N. Watanabe, T. Kimoto, and J. Suda, "The temperature dependence of the refractive indices of GaN and AlN from room temperature up to 515°C", *J. Appl. Phys.* 104 (10), 106101 (2008).

[14] J.-F. Carlin et al., "Progresses in III-nitride distributed Bragg reflectors and microcavities using AlInN/GaN materials", *Phys. Stat. Sol. B* 242 (11), 2326–2344 (2005).

[15] M. Kuramoto, C. Sasaoka, N. Futagawa, M. Nido, and A.A. Yamaguchi, "Reduction of internal loss and threshold current in a laser diode with a ridge by selective re-growth (RiS-LD)", *Phys. Stat. Sol. A* 192 (2), 329–334 (2002).

[16] Y. Oshima, T. Yoshida, K. Watanabe, and T. Mishima, "Properties of Ge-doped, high-quality bulk GaN crystals fabricated by hydride vapor phase epitaxy", *J. Cryst. Growth* 312 (24), 3569–3573 (2010).

[17] D. Brunner et al., "Optical constants of epitaxial AlGaN films and their temperature dependence", *J. Appl. Phys.* 82 (10), 5090–5096 (1997).

[18] Y. Oshima et al., "Thermal and optical properties of bulk GaN crystals fabricated through hydride vapor phase epitaxy with void-assisted separation", *J. Appl. Phys.* 98 (10), 103509 (2005).

[19] C.J. Deatcher et al., "In situ optical reflectometry applied to growth of indium gallium nitride epilayers and multi-quantum well structures", *Semicond. Sci. Technol.* 18 (4), 212–218 (2003).

[20] M.J. Bergmann and H.C. Casey Jr., "Optical-field calculations for lossy multiple-layer $Al_xGa_{1-x}N/In_xGa_{1-x}N$ laser diodes", *J. Appl. Phys.* 84 (3), 1196–1203 (1998).

[21] H.P. Zhou, W.Z. Shen, H. Ogawa, and Q.X. Guo, "Temperature dependence of refractive index in InN thin films grown by reactive sputtering", *J. Appl. Phys.* 96 (6), 3199–3205 (2004).

[22] R. Sarzała et al., "Numerical self-consistent analysis of VCSELs", *Adv. Opt. Technol.* 2012, 689519 (2012).

[23] S.S. Konoplev, K.A. Bulashevich, and S.Yu. Karpov, "From large-size to micro-LEDs: scaling trends revealed by modeling", *Phys. Stat. Sol. A* 215 (10), 1700508 (2018).

[24] M.M. Mensi et al., "Direct measurement of nanoscale lateral carrier diffusion: toward scanning diffusion microscopy", *ACS Photonics* 5 (2), 528–534 (2018).

[25] R. Aleksiejūnas et al., "Carrier transport and recombination in InGaN/GaN heterostructures, studied by optical four-wave mixing technique", *Phys. Stat. Sol. C* 0 (7), 2686–2690 (2003).

[26] P. Ščajev, K. Jarašiūnas, S. Okur, Ü. Özgür, and H. Morkoç, "Carrier dynamics in bulk GaN", *J. Appl. Phys.* 111 (2), 023702 (2012).

[27] F. Nippert, "Determination of recombination coefficients in InGaN quantum-well light-emitting diodes by small-signal time-resolved photoluminescence", *Jpn. J. Appl. Phys.* 55 (5S), 05FJ01 (2016).

[28] F. Nippert, "Temperature-dependent recombination coefficients in InGaN light-emitting diodes: Hole localization, Auger processes, and the green gap", *Appl. Phys. Lett.* 109 (16), 161103 (2016).

[29] J. Piprek, F. Römer, and B. Witzigmann, "On the uncertainty of the Auger recombination coefficient extracted from InGaN/GaN light-emitting diode efficiency droop measurements", *Appl. Phys. Lett.* 106 (10), 101101 (2015).

[30] P. Tian, "Temperature-dependent efficiency droop of blue InGaN micro-light emitting diodes", *Appl. Phys. Lett.* 105 (17), 171107 (2014).

[31] W.G. Scheibenzuber, "Recombination coefficients of GaN-based laser diodes", *J. Appl. Phys.* 109 (9), 093106 (2011).

[32] M. Monavarian et al., "Explanation of low efficiency droop in semipolar (2021) InGaN/GaN LEDs through evaluation of carrier recombination coefficients", *Opt. Express* 25 (16), 19343–19353 (2017).

[33] D.S. Meyaard et al., "On the temperature dependence of electron leakage from the active region of GaInN/GaN light-emitting diodes", *Appl. Phys. Lett.* 99 (4), 041112 (2011).

[34] R. Zhou et al., "Steady-state recombination lifetimes in polar InGaN/GaN quantum wells by time-resolved photoluminescence", *Jpn. J. Appl. Phys.* 58 (SC), 05FJ01 (2016).

[35] A. Dmitriev and A. Oruzheinikov, "The rate of radiative recombination in the nitride semiconductors and alloys", *J. Appl. Phys.* 86 (6), 3241–3246 (1999).

[36] S.Yu. Karpov, "Effect of localized states on internal quantum efficiency of III-nitride LEDs", *Phys. Stat. Sol. RRL* 4 (11), 320–322 (2010).

[37] Ł. Piskorski, L. Frasunkiewicz, and R.P. Sarzała, "Comparative analysis of GaAs- and GaSb-based active regions emitting in the mid-infrared wavelength range", *Bull. Pol. Ac.: Tech.* 63 (3), 597–603 (2015).

[38] Y.C. Shen, G.O. Mueller, S. Watanabe, N.F. Gardner, A. Munkholm, and M.R. Krames, "Auger recombination in InGaN measured by photoluminescence", *Appl. Phys. Lett.* 91 (14), 141101 (2007).

[39] M. Zhang, P. Bhattacharya, J. Singh, and J. Hinckley, "Direct measurement of auger recombination in $In_{0.1}Ga_{0.9}N$/GaN quantum wells and its impact on the efficiency of $In_{0.1}Ga_{0.9}N$/GaN multiple quantum well light emitting diodes", *Appl. Phys. Lett.* 95 (20), 201108 (2009).

[40] H. Fu, Z. Lu, and Y. Zhao, "Analysis of low efficiency droop of semipolar InGaN quantum well light-emitting diodes by modified rate equation with weak phase-space filling effect", *AIP Adv.* 6 (6), 065013 (2016).

[41] P. Li, Y. Zhao, X. Yi, and H. Li, "Effects of a reduced effective active region volume on wavelength-dependent efficiency droop of InGaN-based light-emitting diodes", *Appl. Sci.* 8 (11), 2138 (2018).

[42] T. Swietlik, G. Franssen, R. Czernecki, M. Leszczynski, C. Skierbiszewski, I. Grzegory, T. Suski, P. Perlin, C. Lauterbach and U.T. Schwarz, "Mode dynamics of high power (InAl)GaN based laser diodes grown on bulk GaN substrate", *J. Appl. Phys.* 101 (8), 083109 (2007).

[43] M. Malinverni et al., "InGaN laser diodes emitting at 500 nm with players grown by molecular beam epitaxy", *Appl. Phys. Express* 8 (2), 022105 (2015).